Measurements and Modeling of Effects of Out-of-Plane Reverberation on the Power Delay Profile for Underwater Acoustic Channels

Trond Jenserud and Sven Ivansson

***Abstract*—Long reverberation tails are often observed in shallow-water acoustic channel impulse responses (CIRs). Examples from three significantly different environments along the Norwegian coast are presented. It is shown that 2-D propagation modeling fails to reproduce the long tails. Nevertheless, inclusion of the impulse response tails is necessary in connection with model-based simulators of communication performance, to avoid too optimistic estimates of bit error rates, etc. This is demonstrated by simulation examples for one of the environments, comparing results for truncated and complete impulse responses. High wind speeds and Doppler spread signals indicate that surface reverberation must be taken into account for modeling the tail energy. In bistatic scenarios such as the ones considered here, backscattering computations in a single vertical 2-D plane are not sufficient. A 3-D ray-based model, Rev3D, is utilized to include effects of out-of-plane scattering from the sea bottom as well as the sea surface. The scattering-strength functions include azimuthal variation, with significantly enhanced scattering close to the forward direction. Rev3D modeling supports the hypothesis that out-of-plane scattering and reverberation are main mechanisms behind the observed continuous, exponentially decaying impulse responses. Modeling incorporates available environmental information concerning sound-speed profiles, bottom topography and type, surface wave spectra, etc. Good agreement of measured and modeled time series is obtained for two of the locations. For the remaining location, modeling correctly recovers a significantly lower decay rate of the reverberation tail in comparison to the other locations, but the modeled decay rate is somewhat too large.**

***Index Terms*— Multipath channels, propagation, scattering, underwater acoustic communication.**

I. Introduction

SIMULATIONS of underwater acoustic communication (UAC) channels are useful for several reasons. They allow testing of new modulation schemes and receiver algorithms to be done in the laboratory, thus saving expensive sea trials, avoiding uncertainties due to inaccurate or unknown environmental parameters, and ensuring that comparison of different methods/modulations is made under identical conditions. In the laboratory, simulations can run for as long a time as required without the limitation imposed by the finite stationarity time of the ocean channel, or other practicalities. This is useful for, e.g., bit-error-rate (BER) simulations.

Channel simulators may be driven by data [1], or be model based. Realistic channel mimicry based on modeling is very challenging, but allows simulation of unmeasured channels. There exist several approaches to physics-based modeling, including deterministic [2], [3] and stochastic [4], [5] methods as well as methods based on deriving statistical properties from physics [6]. These approaches usually rely on some propagation model to determine, for instance, propagation delay and loss. The most flexible methods for channel modeling are based on direct simulation of time-varying environments [7]. Physics-based models may include the effects of attenuation, noise, multipath, Doppler effects due to platform motion and surface waves, as well as effects of bubbles [8].

A basic requirement for model-based simulators is the ability to realistically model the power delay profile (impulse response) of the channel. This is not a trivial task, as was shown by Simons *et al.* [9], and verified by our own measurements. The inability to model all aspects of the delay profile may result in unrealistic simulation performance, as was demonstrated by Jenserud and Otnes [10]. This finding is the main motivation behind the present work; in order to improve the fidelity of model-based simulation more accurate modeling of the channel impulse response (CIR) is needed.

The Norwegian Defence Research Establishment (FFI, Horten, Norway) has carried out measurements of the acoustic channel in several shallow-water environments [11]. A characteristic feature often found in the CIRs is long continuous tails. These tails are not reproduced by simple 2-D propagation modeling, even with good environmental knowledge. The origin of the continuous tails is not perfectly clear; however, the frequency spread experienced indicates that scattering from the sea surface is involved, and with a wind speed of about 10 m/s or more during some of the measurement period, bubbles may also contribute to scattering.

Scattering from the sea surface is a 2-D problem, giving rise to out-of-plane effects; due to the 2-D nature of the sea surface, reflections and scattering from patches outside the vertical source–receiver plane may reach the receiver. Taking this into account requires 3-D acoustic computations. Bistatic reverberation calculations further require 3-D scattering functions for both the sea surface and sea bottom.

Manuscript received February 01, 2015; revised June 06, 2015; accepted September 02, 2015. Date of publication September 21, 2015; date of current version October 09, 2015. This work was presented in part at the 2014 Conference on Underwater Communications and Networking (UComms), Sestri Levante, Italy, Sep. 2014.

Associate Editor: J. Potter.

T. Jenserud is with the Norwegian Defence Research Establishment (FFI), Horten NO-3191, Norway (e-mail: trond.jenserud@ffi.no).

S. Ivansson is with the Swedish Defence Research Agency (FOI), Stockholm 164 90, Sweden (e-mail: sven.ivansson@foi.se).

Digital Object Identifier 10.1109/JOE.2015.2475675

0364-9059 © 2015 IEEE. Translations and content mining are permitted for academic research only. Personal use is also permitted, but republication/redistribution requires IEEE permission. See http://www.ieee.org/publications_standards/publications/rights/index.html for more information.

Although backscattering from the sea surface and the sea bottom has been extensively measured (see, e.g., [12, ch. 8]) and [13] for reviews), little data are available on out-of-plane scattering. In lack of measurements, general scattering functions have been constructed as extrapolations from only backscattered information. Ellis and Crowe [14] describe an essentially phenomenological bistatic scattering function, combining isotropic Lambert's scattering with a function of Kirchhoff approximation type that is concentrated near the direction of specular reflection. Physics-based scattering functions have also been proposed, such as the composite roughness model and the small slope approximation. Dahl [15] uses the small slope approximation to compute the bistatic cross section of the sea surface, and Choi and Dahl [16] compute CIRs in a range-independent case, using ray-tracing and bistatic scattering functions based on the small slope approximation. For modeling the impulse response of communication channels, a correct treatment of near-specular scattering is important, since a significant contribution to reverberation probably comes from near forward scattering from an area relatively close to the vertical source–receiver plane.

The purpose of this study is to include the effects of out-of-plane scattering and reverberation in modeling of the CIRs. Time variability is not considered in modeling—the focus is on reproducing the average power delay profile of the channel.

The paper is organized as follows. Section II describes three sea experiments conducted in different locations along the Norwegian coast, and demonstrates the shortcomings of 2-D propagation modeling in reproducing the measured impulse responses. In Section III, we demonstrate, through a simulation study, that neglecting the continuous tail of the CIRs results in too optimistic estimates of communications performance. These sections serve as the motivation for the 3-D modeling that follows in Sections IV–VI. A model with the capability of computing propagation and reverberation for a bistatic geometry, the 3-D ray-based Rev3D, is described in Section IV. An important component of the model is the scattering strength functions for the sea surface and the sea bottom. A semiempirical model and a physics-based scattering model are compared. Modeling results for the three locations are given in Sections V and VI. Finally, the wind-speed dependence of the data is investigated in Section VII, and compared with modeling. Section VIII summarizes our findings.

II. Underwater Acoustic Channels and Their Properties: Three Examples

Channel measurements carried out by FFI over the past few years have revealed a large variety of channels [17]. There seems to be no such thing as a typical channel; shallow-water communication channels range from stable single path propagation to heavily overspread. The channels may be characterized as (quasi)stationary, cyclostationary, or nonstationary. Impulse responses may have sparse or dense arrival structures.

In the following, three examples of channels measured at different locations along the Norwegian coast are considered. The left panels of Fig. 1 display CIRs, while the right panels show transmission loss in the corresponding environments. The source–receiver ranges are similar, about 900 m, for all three cases.

Location A is an open fjord environment, with source and receiver mounted on shallow seamounts with a deeper trough in between. Wind is measured at a nearby shore station, but the local topography may influence wind measurements for some wind directions. Bottom properties are not well known; close to the receiver the bottom is hard, with outcrops of rock and patches of sand, while toward the transmitter there are softer sediments. Sound-speed profiles measured during the trial revealed the presence of a surface channel (cf., Fig. 1), with clear variations from day to day.

Location B is a continental shelf area with a fairly flat bottom at 70-m depth. Wind speed and bottom properties were not measured during the trial, and are estimated from marinograms (forecasts), and Mareano bottom composition maps, respectively. The sound-speed structure in the area shows significant variability both temporally and spatially. The variability is caused by internal waves on a well-developed pycnocline (steep density gradient).

Location C is inside a fjord with rather complex topography, and the source and the receiver are located on seamounts along a ridge. The bottom properties are relatively poorly known, and there is significant oceanographic variability in the upper 30 m of the water column. Grab samples at various locations in the area indicate a soft surface layer, with an average grain size M_z around 8, but the thickness of the sediment layer is not known.

Although the environments and the measured CIRs are very different for the three locations, there are common features; the long, continuous tail of the impulse responses is the most notable one. The total length of the tails is not even captured by the probe signals employed, at least for locations A and B; hence the signal does not reach the noise floor before the onset of a new probe.

The probe signals used for the analysis are linear frequency modulation (LFM) chirps, where the length of the signal is adapted to the delay and Doppler spread of the channel. Each probe consists of a number of repetitions. For location A, the probe consists of 256 repetitions of a 128-ms LFM chirp with center frequency 14 kHz and bandwidth 8 kHz. Location B uses the same bandwidth and center frequency, but the probe consists of 18 repetitions of a 512-ms LFM chirp in this case. For location C, 64 repetitions of a 256-ms LFM signal centered at 6 kHz with bandwidth 4 kHz is used. The measured CIRs are obtained by averaging over all pings within a probe. The different number of repetitions of the probes leads to different variances in the measured impulse responses, as is evident from Fig. 1.

The measured impulse responses are much smoother than the modeled ones. One reason for the differences is the averaging that takes place in the measurements; another reason is that signal processing is not included in modeling.

A. Two-Dimensional Propagation Modeling

An attempt to model the impulse responses by the 2-D ray tracer LYBIN [18] is shown by the gray curves in Fig. 1. The overall picture is that modeling is not very successful. Most striking is the lack of the model to reproduce the continuous tails found in the data; the modeled arrivals are too sparse and decay

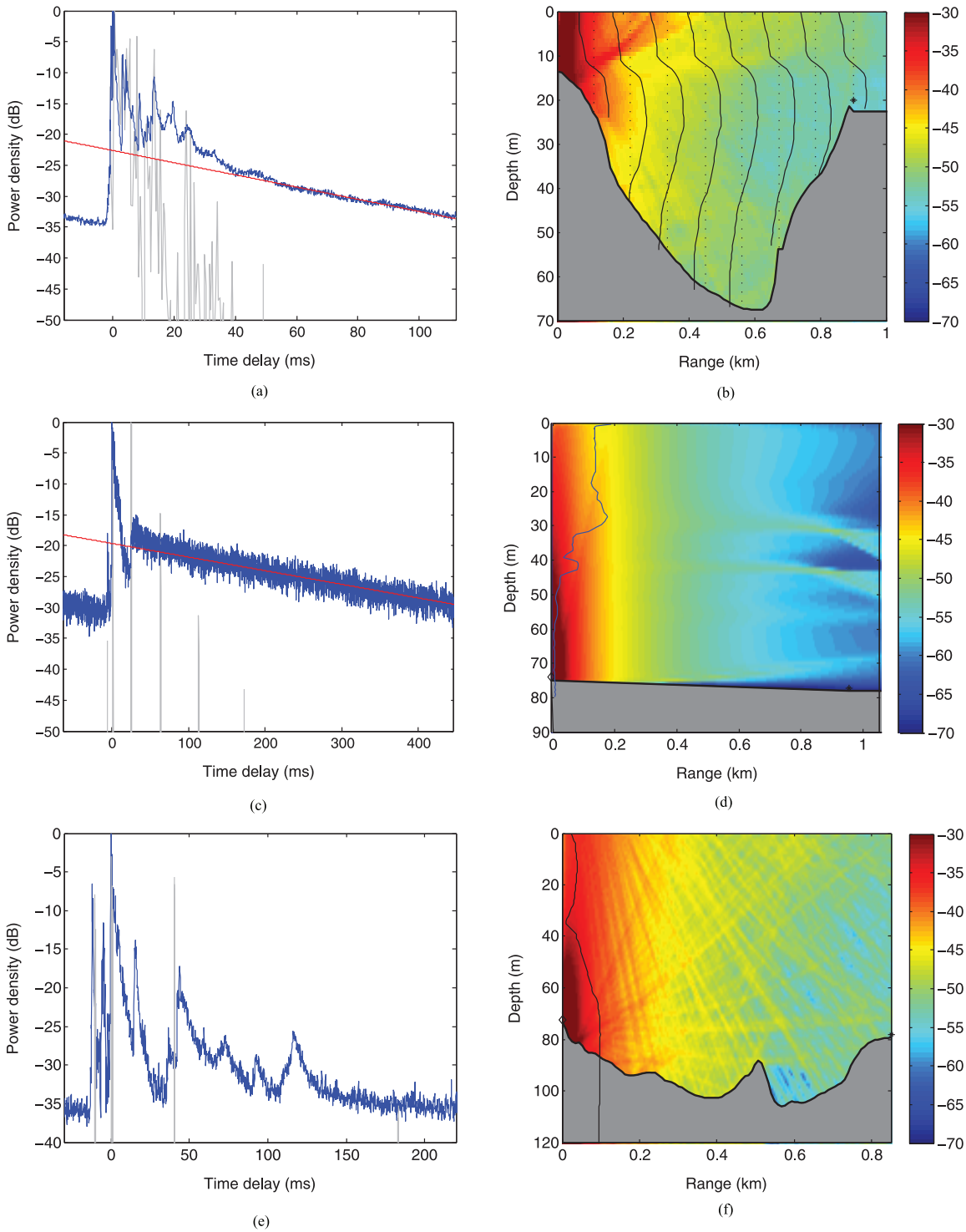

Fig. 1. Left panels show measured (blue) and modeled (gray) power delay profiles for three different locations: A (upper), B (middle), and C (lower). Right panels show sound-speed profile shapes (black) and transmission loss (TL) in the environments. TL is in dB re 1 m^2, and is computed with LYBIN. The center frequencies for the measurements are 14 kHz for locations A and B, and 6 kHz for location C. Time delay is relative to the surface-reflected path.

too fast. But even in the discrete part of the responses (the multipath arrivals), although the overall arrival structure is captured, there are significant discrepancies in the relative amplitudes of the arrivals. Among the reasons for the modeling difficulties are the complex topography of locations A and C, and also the fact that for all three locations the source and the receiver are located very close to the bottom, which gives rise to shadowing effects and high sensitivity for bottom topography.

1) Location A: The arrival structure of location A is very complex. The direct and first surface bounce arrive within 1 ms, followed at delay time $\tau = 5$ ms by a group of arrivals with two surface reflections. A notable peak at $\tau = 15$ ms corresponds to paths with three surface reflections. Reflection from the variable topography contributes to intermediate arrivals. Despite the complexity of the problem, several of the more pronounced peaks are reproduced reasonably well.

2) Location B: The impulse response of location B apparently consists of a few arrivals followed by a very long tail. Modeling reveals a more complex picture; the arrivals are clustered in widely separated groups, each group corresponding to rays with the same number of surface reflections, and up to two bottom reflections close to the source and receiver. Each group of arrivals seems to give rise to a decaying tail, where the decay rate decreases with an increasing number of surface reflections. The strongest arrival at $\tau = 0$ ms is the first surface-reflected path, while each following arrival group corresponds to one more surface reflection. The relative amplitudes of the arrival groups are not correctly modeled; the angle dependence of the surface-reflection coefficient seems incorrect, and again modeling fails completely in reproducing the dense tail. A weaker direct arrival can also be seen at $\tau = -3$ ms. One would not expect the direct arrival to be weaker than the surface-reflected path. However, observation over some hours reveals that this arrival fades in and out, being sometimes stronger than the surface-reflected path. There are two probable reasons for the fading. 1) Both source and receiver are very close to the bottom ($\sim$1 m); slight changes in the sound-speed profile may therefore cause the receiver to come into a shadow zone. 2) Modeling indicates that the arrival actually consists of a direct plus bottom-reflected path of almost the same path length, which may then result in interference effects.

3) Location C: Location C shows a complicated arrival picture, with arrivals coming in at large separations, each followed by a decaying tail. Although the model predicts some of the arrivals correctly, it misses some rather pronounced arrivals, and again fails completely in reproducing the continuous parts of the impulse response. More specifically, eight significant peaks are seen in the measurement, located at $\tau = -12$, -6, 0, 20, 45, 70, 90, and 120 ms. Only peaks 1, 3, 5, and 6 are captured by the 2-D model. Arrival 1 corresponds to a direct plus bottom path. The next arrivals consist of groups of close arrivals with up to two bottom reflections close to the source and receiver, respectively. Arrival 3 has one surface reflection, arrival 5 has two surface reflections and one bottom reflection, and arrival 6 has two surface reflections and two bottom reflections.

B. Properties of the Reverberant Tails

The continuous tails of the impulse responses are now examined in more detail. The first thing to note is that the tails decay close to exponentially. This is shown by the red curves in Fig. 1, which are exponentials fitted to the tails. Interestingly, the decay rates are very different for the different areas: -10 dB/100 ms for location A, -2.6 dB/100 ms for location B, while for location C several decay rates are experienced. Modeled propagation also decays faster than the measured CIR, indicating the presence of reverberation. The tails show significant Doppler spread, which is an indication of surface interaction. The Doppler spread seems to increase with increasing delay time. The covariance matrix indicates some correlation for the discrete arrivals in the first part of the signal, while the tail is essentially uncorrelated. Further, the scaled residual $(y - y_{\text{fit}})/y_{\text{fit}}$ has a (close to) Gaussian amplitude distribution. These properties are illustrated in Fig. 2 for relatively low wind conditions in location A. Doppler sidebands, corresponding to the peak wave period are also observed in the data at the lower wind speeds.

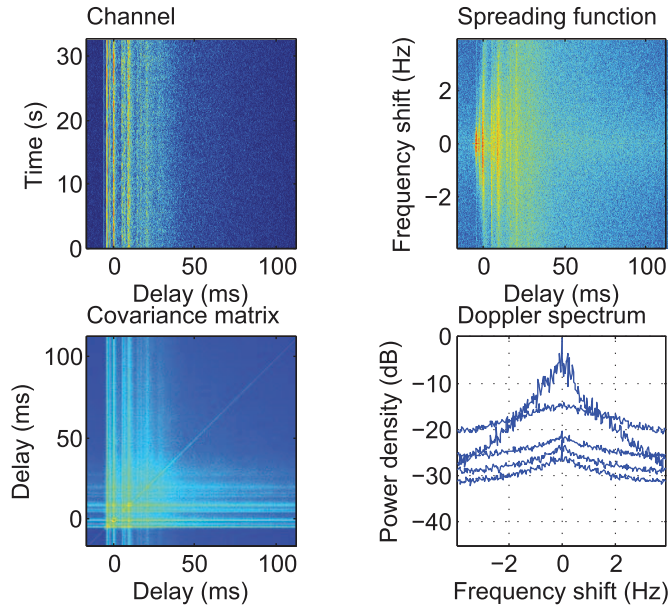

Fig. 2. Properties of CIR for location A. The upper panels show the time-varying impulse response of the channel (left) and the corresponding spreading function (right). The lower right plot is obtained from the spreading function by computing averaged Doppler spectra for five consecutive time segments over the length of the signal. The spectra are shown in the order of increasing delay time from top to bottom. The lower left plot shows the covariance matrix of the impulse response.

For higher winds, the Doppler spectra are even broader, which may result in aliasing in frequency. The effects of frequency aliasing on measured impulse responses depend on the type of probe signal employed. For LFM signals as used here, frequency aliasing causes the multipath arrivals to be broadened, and their amplitude to be reduced relative to the reverberant tail [11].

To obtain better modeling it is necessary to include the physical effects responsible for the long continuous tail. The observations above lead us to believe that scattering from the sea surface plays an important role. For taking this into account properly in bistatic scenarios (typical for communications), characterized by out-of-plane reverberation of the forward-scatter type, 3-D computations are required.

An alternative, and much simpler, approach to modeling is to retain the simple forward model for computing the multipath arrivals, but to use an empirical model for the continuous tail. A work along these lines is [9], which fits parametric models to both discrete and continuous parts of the CIR, assuming the continuous part decays exponentially. The disadvantage of this approach is that the simple parametric models are not generally valid and have to be fine tuned for every environment.

III. Effect of Insufficient Modeling of CIR on Estimated Communication Performance

The quality of a channel simulator can be assessed by its ability to reproduce channel characteristics, such as the average power delay profile and scattering function. More important however, is the simulator's ability to reproduce communication performance.

The presence of long, reverberant tails in the CIR poses challenges for the simulation of communication performance. For measurement-based simulators, the (only) problem of a long tail is that it may lead to reduced quality of the measured CIR due to aliasing in time delay or Doppler. When the simulator is driven by aliased channel measurements, it will indeed reproduce the measured channel, but the predicted communication performance will not be correct.

For model-based simulators, it is already challenging to model the impulse response in a discrete multipath environment, and to include a reverberant tail further increases the requirements on modeling.

The impact of the tail on communication performance depends on receiver properties and parameters, such as equalizer length, etc. However, a long tail will generally act as interference and cause reduced communication performance. Insufficient modeling of the tail is therefore expected to result in too optimistic estimates of communication performance. To demonstrate this effect, simulations using the Mime channel simulator [1] on channel measurements from location A are considered.

The simulations are performed by passing six different communication waveforms through the channel simulator, which is configured to run in stochastic replay mode (mode 2). This mode provides multiple realizations of the channel with the same statistical properties as a provided channel measurement. Three different channel measurements are provided to the simulator as shown in Fig. 3: the full measured CIR, a truncated version where the reverberant tail (the green part) is cut off, and a CIR where only the peaks are extracted. The rationale for the latter is that the peaks correspond to discrete multipath arrivals, and thus represent the best possible performance of a conventional 2-D ray-trace model. This approach is also a simple method of cutting away all reverberant energy. A number of 100 packets are transmitted through 100 different realizations of the channels, the resulting signals are then demodulated, and the resulting packet error rate (PER) and BER are computed. The simulations show, as expected, that cutting away the reverberant tail leads to too optimistic performance estimates. By including only the peaks of the CIR (representing the multipath arrivals), the estimation errors are further increased.

It is concluded that model-based simulations tend to overestimate communication performance when reverberant energy is not included in modeling. As remarked above, sea-surface scattering appears to be an important source of reverberation. In bistatic scenarios with complex bottom topography, 3-D acoustic computations are needed to model the scattering, including its out-of-plane contributions. Sections IV–VII deal with efforts to model the whole CIR by such 3-D computations.

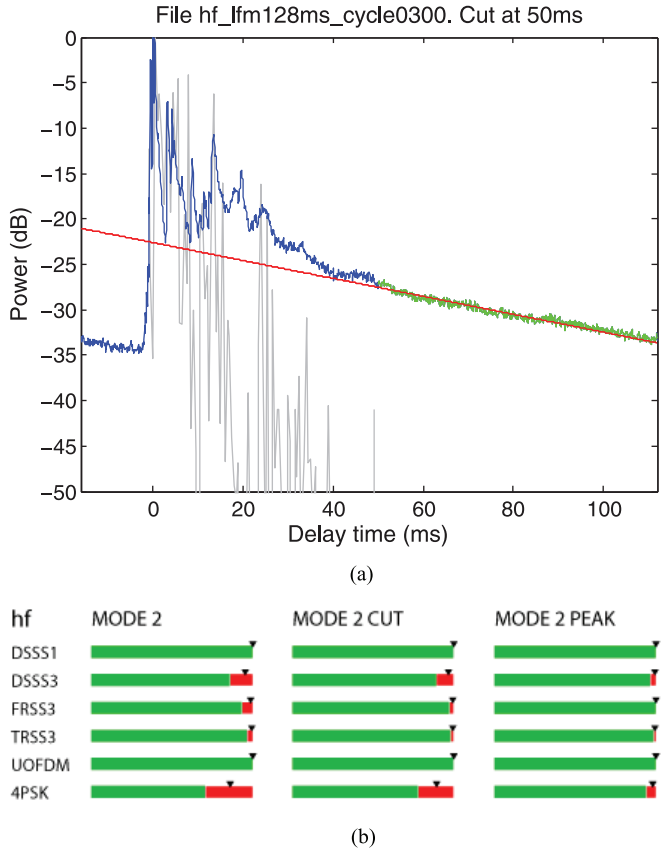

Fig. 3. (a) Power delay profile (blue and green) for location A with overlaid model results (gray). An exponential fit to tail is shown by the red curve. The green part of the profile is the tail that is cut away. (b) PER and average BER (black triangles) for Mime mode 2 on original CIR (left), truncated CIR (middle), and CIR consisting of extracted peaks (right). The amount of green in the horizontal bars represents the fraction of packets received without errors. The black triangle represents the BER, averaged over the 100 packets, on a linear scale from 0.5 on the left to 0 on the right. The communication waveforms employed are (from top): Four variants of spread spectrum, orthogonal frequency-division multiplexing (OFDM), and phase-shift keying (PSK). The figure is reproduced from [10].

IV. Three-Dimensional Propagation and Reverberation Modeling

Rev3D is a 3-D ray-based model for computation of propagation-loss curves as well as time series for reverberation and propagation [19], [20]. In particular, rays from the source are traced with different azimuths as well as elevations.

The sound speed in the water is represented by range-independent profiles within horizontal rectangles. In each rectangle, the variation of the sound speed c with depth is approximated to be of the "$1/c^2$ piece-wise linear" type. Hence, each ray is built up as a sequence of parabolic arcs. Bottom depths are given explicitly at the grid points for the horizontal rectangles, and bilinear interpolation is used in between. The intersections of a ray with the bottom can be calculated quickly by solving second-degree polynomial equations.

All energy flow is confined to the thin rays, as in [21], and ray diagrams are produced. The average intensities in Rev3D are computed for receiver box volumes, obtained by a polar grid centered at the source in the horizontal plane and a division of the depth axis. Each ray contributes to the average for a particular box according to the energy it carries and its arc length within that box. Propagation loss curves can be produced in selected bearing directions from the source. The propagated energy is positioned on a time axis, and time traces for pressure magnitude space averages in the different receiver boxes can also be obtained.

Bottom and surface reverberations are treated separately, based on computation of average intensities at interface patches. These patches or area elements are formed from another polar grid, now centered at the receiver.

Rev3D has an option to use general scattering-strength functions, but the computational speed is enhanced significantly with separable functions allowing source-to-patch and patch-to-receiver terms to be summed separately for each patch. In this paper, contributions from different rays are added incoherently (power sums), but options for coherent computations have also been developed [22].

A. Reflection Coefficients

Rays are reflected specularly at the sea bottom and at the sea surface, and the reflection coefficients are functions of grazing angle and frequency. The bottom-reflection coefficients additionally depend on the bottom type, while the surface-reflection coefficients additionally depend on the wind speed.

For each horizontal grid rectangle, the bottom type can be specified as a porosity value or as a layered bottom with geoacoustic parameters for the different layers. In the former case, which is used in the modeling examples in this paper, the bottom-reflection coefficients R are computed from an empirical formula [23]. Fig. 4 shows two examples, which are relevant for modeling of locations A and B and location C, respectively.

In reality, losses are induced by an absorbing layer of bubbles beneath the sea surface [24]. The bubble density and depth distribution depend on the wind speed. For simplicity, the losses are included in an effective reflection coefficient, for which an expression in [25, Sec. 8.1.1.2.2], originating from work by Peter Dahl, is here followed. Fig. 4 includes two examples. In contrast to the bottom losses, the bubble-induced surface-reflection losses are the largest for small grazing angles. A loss limit of 15 dB is imposed, because some sound is reflected by the bubble cloud before being absorbed by it.

B. Intensity Time Traces for Reverberation

Bottom and surface reverberations are handled analogously. In each case, the reverberation time trace for intensity is built up by contributions from each interface patch. Focusing on a particular patch with area $\mathrm{d}A$, its contribution $\varphi(t)$ at time t for a Dirac intensity pulse $\delta(t)$ from the source can be written as

$$\varphi(t) = \sum_u \sum_v T_u \, R_v \, S_{u,v} \, \delta(t - t_{\mathrm{T},u} - t_{\mathrm{R},v}). \qquad (1)$$

The sums on u and v are for the transmit (from the source to the patch) and receive (from the patch to the receiver, but by reciprocity computed from the receiver to the patch) ray paths, respectively. The corresponding travel times are denoted $t_{\mathrm{T},u}$ and $t_{\mathrm{R},v}$. T_u is the average intensity over the patch contributed by ray u multiplied by $\sqrt{\mathrm{d}A}$. R_v is defined analogously, while $S_{u,v}$ is the scattering strength (per unit boundary area, 1 m^2), for the ray angles involved.

Apparently, the product $T_u \, R_v$ in (1) takes care of the propagation loss in the appropriate way. For the monostatic case, the factors T_u and R_u for a particular ray differ only because of possibly different transmit and receive beam patterns. For separable scattering kernels, such as the Lambert and Chapman–Harris rules, e.g., [25], $S_{u,v}$ in (1) can be factorized as $S_{u,v} = s_{\mathrm{T},u} \, s_{\mathrm{R},v}$, with transmit and receive factors $s_{\mathrm{T},u}$ and $s_{\mathrm{R},v}$, respectively.

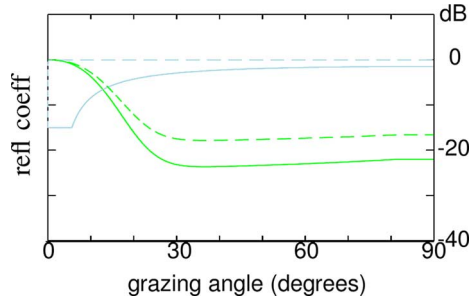

Fig. 4. Reflection coefficients $R = R(\theta)$ at bottom (green) and surface (blue) as a function of grazing angle θ. The solid green and blue curves are relevant for locations A and B, with the frequency of 14 kHz and the wind speed of 10 m/s. The dashed green and blue curves represent location C, with the frequency of 6 kHz and the wind speed of 3.5 m/s. In both cases, the bottom has medium porosity (0.63).

Reverberation time traces are formed by incoherent summation of intensity contributions from each patch. For a source intensity pulse $s(t)$, $\varphi(t)$ is simply convolved with $s(t)$, symbolically $\varphi \star s(t)$. The patches should be small enough to map out possible shadow zones, and to provide closely spaced patch points of transmit and receive rays for an accurate positioning in time of the reverberation energy. The number of rays should be large enough to give an adequate coverage of the patches with rays of different types.

A drawback with (1) is that data for all rays reaching the patch must be stored in order for the double summation to be performed at the end. Moreover, the double summation for each patch for a large number of bottom as well as surface patches requires significant computer time. Approximations are thus of great interest. As discussed in [19], useful approximations can be obtained by splitting the rays for each particular patch into groups, according to travel time or the number of interface reflections, for example. For nonseparable scattering kernels, the ray groups may be designed in terms of grazing angles, for example, to allow reasonably accurate approximations $\tilde{S}_{u,v} = \tilde{s}_{\mathrm{T},u} \, \tilde{s}_{\mathrm{R},v}$ for the different ray-group pairs. Basically, the idea is to replace the double summation on u and v by single summations that can be performed as the ray tracing proceeds without storing data for individual rays.

C. Semiempirical Scattering Kernels

Ellis and Crowe [14] proposed 3-D scattering-strength functions S with two terms, the first for diffuse scattering and the second for facet scattering, for sea bottom as well as sea-surface reverberation. Specifically

$$S(\theta_1, \theta_2, \beta) = S_0(\theta_1, \theta_2) + \nu(1 + \Delta\Omega)^2 \exp(-\Delta\Omega/2\sigma^2) \qquad (2)$$

where θ_1 and θ_2 are grazing angles for incoming and outgoing rays, respectively, and β is the angle as viewed from the patch between the projections on the patch plane of the incoming and outgoing rays. The quantity $\Delta\Omega$ is a certain function of the three angles θ_1, θ_2, and β, which vanishes for the specularly reflected ray (with $\beta = 180^\circ$ and $\theta_2 = \theta_1$), while ν and σ are facet-strength and facet-slope parameters, respectively. $\Delta\Omega$ is symmetric in θ_1 and θ_2.

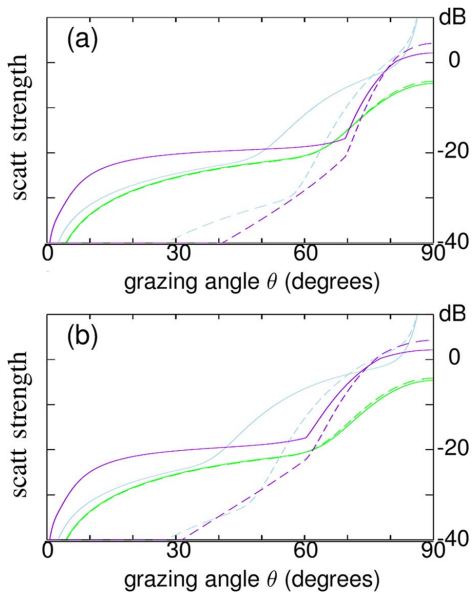

Fig. 5. Some scattering strength function $S(\theta, \theta, \beta)$ for the sea bottom (green) and for the sea surface (blue and violet for the semiempirical and composite roughness scattering models, respectively). The bistatic angle β equals 0° in (a), backscattering, and 90° in panel (b). For the solid curves, relevant for locations A and B, the frequency is 14 kHz and the wind speed is 10 m/s. The dashed curves, for a frequency of 6 kHz and a wind speed of 3.5 m/s, are relevant for location C. The bottom has medium porosity (0.63) with roughness slope angle ϕ equal to 7°.

The second term in (2) concerns facet scattering, and it can be derived from the Helmholtz integral with the Kirchhoff approximation for a rough boundary. This term includes a dependence on the bistatic angle β, allowing scattering in the forward direction to be stronger than scattering in the backward direction.

For the bottom, Ellis and Crowe [14] suggested Lambert's rule for the first term $S_0(\theta_1, \theta_2)$ in (2). This choice gives a separable term, in the sense that $S_0(\theta_1, \theta_2) = [S_0(\theta_1, \theta_1)]^{1/2}[S_0(\theta_2, \theta_2)]^{1/2}$. In this paper, S_0 for the bottom is somewhat different. While still separable, it depends on the bottom porosity according to empirical curves. Concerning the parameters ν and σ for the bottom, Ainslie [25, Sec. 8.1.4] has suggested $\sigma = \tan(\phi)$, where ϕ is a roughness slope angle, and

$$\nu = \frac{|R(\theta_1)|^2}{8\pi\sigma^2} \tag{3}$$

where $R(\theta_1)$ is the bottom-reflection coefficient at the grazing angle θ_1 of the incoming ray. Apparently, the resulting $S(\theta_1, \theta_2, \beta)$ is not symmetric in θ_1 and θ_2. The green curves in Fig. 5 show some examples of bottom-scattering kernels S, when the grazing angles θ_1 and θ_2 are equal.

For the surface, the empirical Chapman–Harris separable backscattering kernel, bounded below by a perturbation theory reference used by Ogden and Erskine [26, p. 751], is adopted for S_0. Following [14], parameters ν and σ are in this case taken according to $\sigma^2 = 0.003 + 0.00512v$, where v is the wind speed in meters per second, and $\nu = (8\pi\sigma^2)^{-1}$. The blue curves in Fig. 5 show some examples of surface-scattering kernels S.

D. Composite Roughness Surface Scattering Kernel

Physically-based alternatives to the semiempirical equation (2) have been proposed, which involve statistical roughness information. In particular, the small-slope approximation is a good choice for the bistatic cross section of a rough surface. For the case of sea-surface scattering, it is discussed in [15] and applied in [16] to model impulse responses with several distinguishable surface–bottom bounce arrivals.

In this paper, however, a version of the composite roughness model for surface scattering is considered, which is more easily implemented. It can be expressed as

$$S(\theta_1, \theta_2, \beta) = S_{\mathrm{b}}(\theta_1, \theta_2) + S_{\mathrm{rf}}(\theta_1, \theta_2, \beta) \tag{4}$$

where $S_{\mathrm{b}}(\theta_1, \theta_2)$ is a contribution from bubbles that does not depend on β, and $S_{\mathrm{rf}}(\theta_1, \theta_2, \beta)$ is obtained by interpolation according to [27] of roughness scattering and facet scattering. The bubble contribution S_{b} is taken from [15, eq. (13)], but with the second term doubled to achieve consistency with the monostatic case in [28, eq. (13)] and [29], with parameters (depending on the frequency and the wind speed) from [29]. Typically, S_{b} dominates at low grazing angles, and it is symmetric in θ_1 and θ_2. For scattering close to the specular direction, the term S_{rf} agrees with the Ellis–Crowe facet contribution according to (2), whereas S_{rf} agrees with

$$S_{\mathrm{r}}(\theta_1, \theta_2, \beta) = 4k^4 \sin^2(\theta_1) \sin^2(\theta_2) G_1(\theta_1, \theta_2, \beta) \tag{5}$$

for scattering in directions far from the specular direction. Here, k is the wave number in the water, while G_1 is the isotropic 1-D roughness spectrum derived from the gravity-wave frequency spectrum for the sea [25, eq. (8.4)]. For a fully developed sea, the Pierson–Moskowitz frequency spectrum [25, Sec. 8.1.2] is a convenient choice. The JOint North Sea WAve Project (JONSWAP) [30] frequency spectrum provides an alternative for fetch-limited conditions. It has three parameters: significant wave height H_s (four times the root-mean-square wave height), peak period T_p, and peakedness factor γ. The Pierson–Moskowitz spectrum appears as a special case with $\gamma = 1$. In either case, the resulting surface-scattering kernel S is symmetric in θ_1 and θ_2, since all quantities involved, including G_1, are symmetric.

Some examples, using the Pierson–Moskowitz frequency spectrum, are shown by the violet curves in Fig. 5. Compared to the blue curves for the semiempirical kernel, the bubble term S_{b} causes increased scattering for low grazing angles, at least for higher frequencies and wind speeds.

Physically-based alternatives to the semiempirical equation (2) are, of course, of great interest for bottom scattering as well. Judging by observed time variations in the measured impulse responses, however, surface scattering seems to be the most important here.

E. Scattering With Different Grazing Angles for Incoming and Outgoing Rays

Harrison [31], [32] discusses scattering-strength functions $S(\theta_1, \theta_2, \beta)$ that can be written as products with three factors, each depending on only one angle. Assuming that horizontal

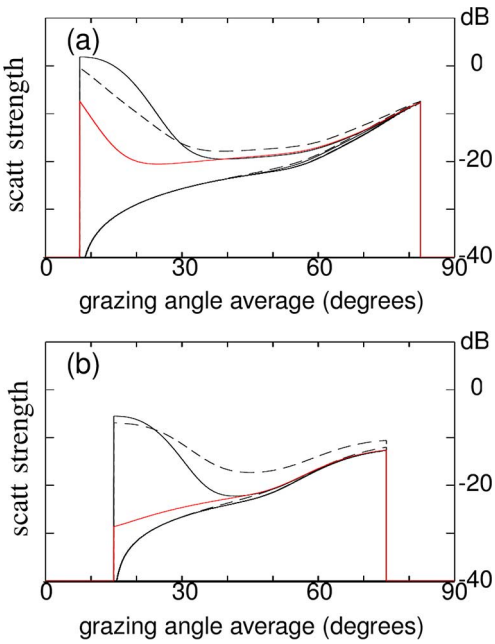

Fig. 6. Scattering strength S for bottom reverberation according to (2) as a function of $(\theta_1 + \theta_2)/2$, for a medium porosity (0.63) bottom with roughness slope angle ϕ equal to 7° at 14 kHz. There are two panels for different values of $|\theta_1 - \theta_2|$: (a) 15° and (b) 30°. In each panel, the dotted curve (often hidden by the lowermost solid curve) shows the separable term S_0, which is independent of β. The five solid curves show results for S, including the facet term for different values of β: 0° (backward direction), 45°, 90°, 135°, and 180° (forward direction), as ordered from the bottom to the top. The five dashed curves show the corresponding approximations $\tilde{S}$ according to (6). Most of the curves are actually very close, with only the uppermost curves, for forward scattering ($\beta = 180°$), clearly different. In each panel, there is also a red curve, which represents the forward-scattered result with ν computed, according to (3), for θ_1 as the largest grazing angle. For the remaining curves, θ_2 is larger than θ_1.

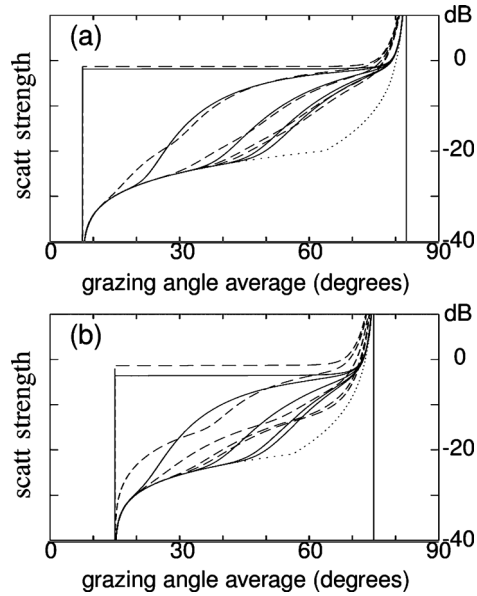

Fig. 7. Scattering strength S for surface reverberation according to (2) as a function of $(\theta_1 + \theta_2)/2$, at 14-kHz frequency and 10-m/s wind speed. As in Fig. 6, there are two panels for different values of $|\theta_1 - \theta_2|$: (a) 15° and (b) 30°. In each panel, the dotted curve shows the Chapman–Harris (together with Ogden–Erskine) separable result S_0, which is independent of β. The five solid and five dashed curves show the results for S and $\tilde{S}$, respectively, in the same manner as in Fig. 6. (Since S is now symmetric in θ_1 and θ_2, there is no need for additional red curves.)

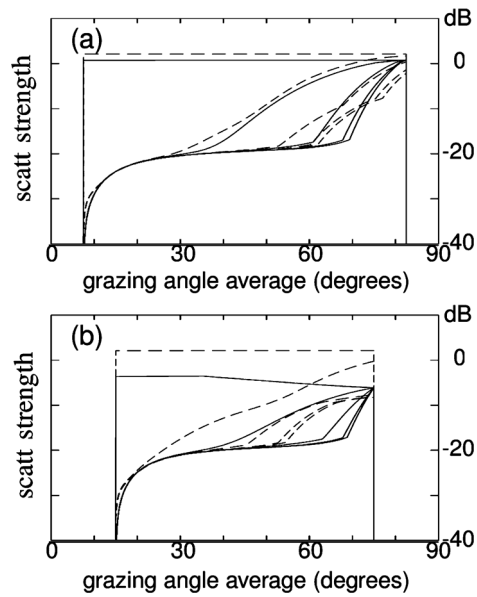

Fig. 8. Scattering strength S for composite roughness surface reverberation according to (4) as a function of $(\theta_1 + \theta_2)/2$, at 14-kHz frequency and 10-m/s wind speed. As in Figs. 6 and 7, there are two panels for different values of $|\theta_1 - \theta_2|$: (a) 15° and (b) 30°. The five solid and five dashed curves show the results for S and $\tilde{S}$, respectively, in the same manner as in Figs. 6 and 7.

refraction of the rays is small, and that the bottom slope at each bottom scattering point is also small, the bistatic angle β can be approximated for each interface patch by the difference $\tilde{\beta}$ of the patch-to-source and patch-to-receiver azimuths. As indicated in Section IV-B, the computer-intensive double summation over u and v in (1) can thereby be avoided by approximations according to [19].

For the kernel S from (2) or (4), a simple partially separable approximation $\tilde{S}$ is obtained by

$$\tilde{S}(\theta_1, \theta_2, \beta) = [S(\theta_1, \theta_1, \beta)\, S(\theta_2, \theta_2, \beta)]^{1/2}. \qquad (6)$$

Indeed, $\tilde{S}$ fulfils $\tilde{S}(\theta_1, \theta_2, \beta) = [\tilde{S}(\theta_1, \theta_1, \beta)\, \tilde{S}(\theta_2, \theta_2, \beta)]^{1/2}$.

For the frequency of 14 kHz, the accuracy of the approximation of (2) according to (6) is illustrated in Figs. 6 and 7. The two figures concern bottom and surface scattering, respectively, with bottom parameters as in Fig. 5 and the wind speed of 10 m/s. Fig. 8 shows the corresponding results for composite roughness scattering according to (4), with the Pierson–Moskowitz frequency spectrum. As noted in connection with Fig. 5, the bubble term S_b causes increased scattering for low grazing angles. Particularly surface scattering is very strong in the forward direction (β close to 180°), for all grazing-angle combinations.

Comparing the dashed curves for the (partially) separable approximation $\tilde{S}$ to the solid curves for S, in Figs. 6–8, it appears, as expected, that the approximation is best when the grazing-angle difference $|\theta_1 - \theta_2|$ is small. For the semiempirical surface scattering kernel (Fig. 7), it appears reasonably satisfactory for the cases shown, with $|\theta_1 - \theta_2| \leq 30°$. For much larger differences, however, $\tilde{S}$ can become a rather poor approximation. Considering the composite roughness scattering kernel (Fig. 8), $\tilde{S}$ may deviate significantly from S already at $|\theta_1 - \theta_2| \leq 30°$ when the grazing-angle average $(\theta_1 + \theta_2)/2$ or the bistatic angle β is large. For the bottom-scattering kernel in Fig. 6, it appears that $\tilde{S}$ differs from S particularly for forward scattering (large

β), and the difference may appear for rather small grazing angles.

Since scattering in the forward direction is important in the examples to follow, full double-sum computations according to (1) are performed.

V. Modeling Results

This section shows some Rev3D modeling results for locations A, B, and C. As detailed in Section II, there is significant uncertainty concerning the environmental parameters, and the bottom properties are poorly known. For modeling in this section, a bottom with medium porosity (0.63) is always assumed, and the roughness slope angle ϕ is taken as 7° (a medium value [25, Sec. 8.1.4.1.3]). Modeling of surface reverberation is done in two ways, with the semiempirical and composite roughness scattering kernels from Sections IV-C and IV-D, respectively, and the results are compared. Comparisons of modeling results to data should focus on the overall shape rather than the absolute level, since calibration information is missing for the measured data. The time signals are now presented as functions of travel time, i.e., delay time from the onset of the source pulse.

Complete computations with double summation according to (1) are made to obtain the contributions to reverberation. In total, some ten million rays are traced from each source and each receiver. The interface patches in the polar grid centered at the receiver have a width of 2° azimuthally and a length of 4 m radially (except close to the receiver where they are smaller).

On a desktop computer, the required central processing unit (CPU) time for a location A case is about 20 h. For test computations with variations of environmental parameters, however, approximations allowing single summations as indicated in Sections IV-B and IV-E are much more convenient, with a reduction of the CPU time to about 1 h. The waiting time could, of course, be reduced by splitting the rays or patches into groups for which the computations could be done in parallel.

A. Location A

Fig. 9 shows Rev3D results for location A, using the alternative with the semiempirical scattering kernel for surface reverberation. The source pulse is centered at 14 kHz and its length, after match-filtering, is 0.125 ms. The wind speed is 10 m/s. Modeled propagation (in gray) plus modeled reverberation (in black, with bottom and surface components in green and blue, respectively) may be compared to the measured data (in violet). A power sum is needed, e.g., [16], to account for reflections and arrivals without boundary interaction (propagation) as well as scattering (reverberation), and the two contribution types have very different geometric spreading.

The propagation modeling, done by fast incoherent 2-D computations, indicates isolated multipath arrivals (in gray) within a time span of about 40 ms, which is consistent with the corresponding LYBIN results and with the measured data (in violet). (Details of the isolated multipath arrivals in Figs. 1 and 9 differ, however, because of slightly different sound-speed profile interpolations and bottom-reflection coefficient computations in LYBIN and Rev3D.) It appears that the initial part of the measured time trace can be explained by ordinary multipath arrivals,

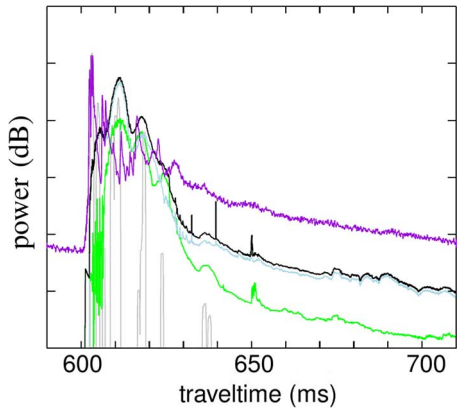

Fig. 9. Modeled and measured time series for location A with 10 dB between thick marks on the vertical axis. Surface reverberation is modeled according to the semiempirical scattering kernel from Section IV-C. The black curve shows modeled total reverberation, while the green and blue curves show the bottom and surface contributions, respectively. There is also a spiky gray curve, which only includes modeled propagation. The violet curve shows the measured data.

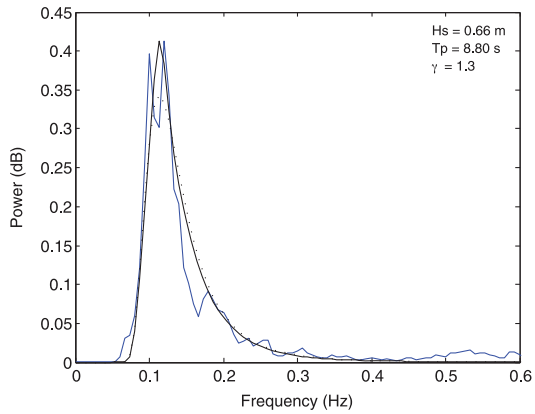

Fig. 10. Measured wave spectrum (blue) with corresponding JONSWAP (solid black) and Pierson–Moskowitz (dashed) wave spectra for location A on October 22, 2014, at 15:00 Z. The measured wind speed is 10 m/s.

and reverberation filling the gaps between the peaks, while reverberation alone accounts for the latter, and more smooth, part. Reverberation appears to be dominated by scattering from the sea surface rather than the sea bottom.

At travel times longer than about 630 ms, the measured as well as modeled data in Fig. 9 drop off smoothly with similar decay rates. The levels of the reverberation-dominated modeling results are too low, however.

A wave-rider buoy was available during these measurements, and Fig. 10 shows the pertinent gravity-wave frequency spectrum, along with corresponding JONSWAP and Pierson–Moskowitz spectra. The JONSWAP parameter values $H_s = 0.7$ m and $T_p = 8.8$ s are obtained from the measured data, while γ is adjusted to 1.3 for best fit. The Pierson–Moskowitz wave spectrum, for the measured wind speed of 10 m/s, is somewhat less sharp, but it also gives a good fit to the measured spectrum.

Fig. 11 shows Rev3D results for location A, using the alternative with the composite-roughness scattering kernel for surface reverberation. The fitted JONSWAP spectrum according to Fig. 10 is here used in connection with (5). Compared to Fig. 9, the main difference is that reverberation drops off at a higher level, closer to the data. Recalling the surface-scattering kernel

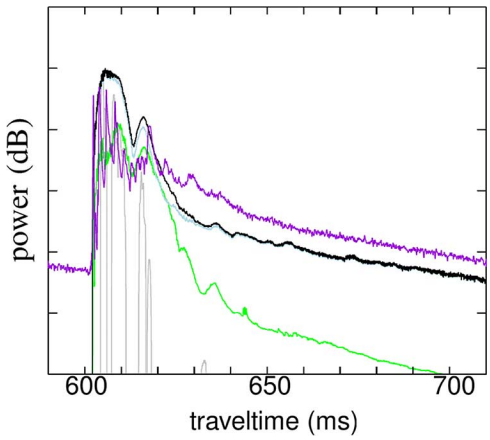

Fig. 11. Modeled and measured time series for location A. The difference from Fig. 9 is that surface reverberation is now modeled according to the composite-roughness scattering kernel from Section IV-D.

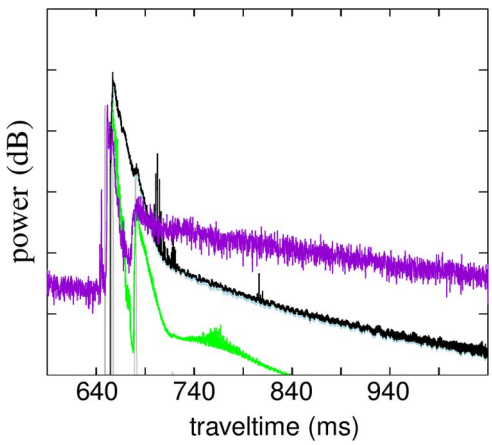

Fig. 12. Modeled and measured time series for location B, with surface reverberation modeled according to the semiempirical scattering kernel from Section IV-C. Again, there are 10 dB between the thick marks on the vertical axis. The black, green, and blue curves represent modeled total, bottom, and surface reverberations, respectively. The gray curve represents propagation, and the violet curve shows the measured data.

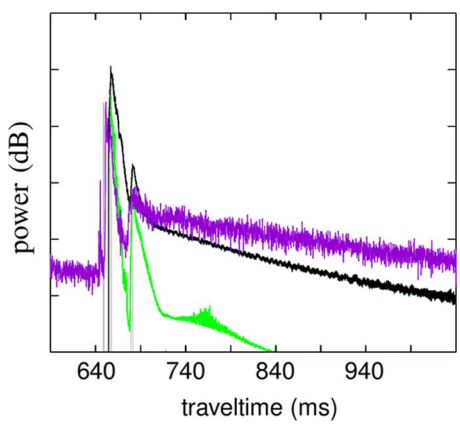

Fig. 13. Modeled and measured time series for location B. The difference from Fig. 12 is that surface reverberation is now modeled according to the composite-roughness scattering kernel from Section IV-D.

curves from Figs. 7 and 8, this is not surprising. The bubble contribution S_{b} of the composite roughness model increases the scattering at the smaller grazing angles, which are typically involved later.

It can also be noted that a few sharp surface reverberation peaks in Fig. 9, at travel times around 640 ms, are virtually absent in Fig. 11. They are probably due to surface scattering involving at least one high angle, for which the semiempirical surface scattering kernel is anomalously large (see Fig. 7).

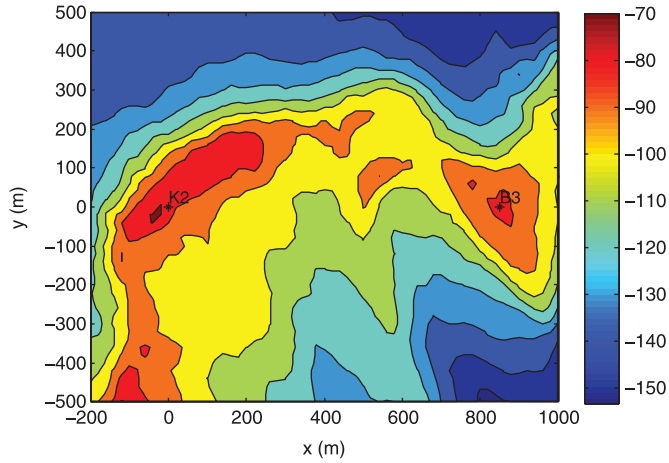

Fig. 14. Bottom topography of location C. The sound source is at position K2 at the origin, while the receiver is at position B3 on the x-axis at $x = 850$ m.

B. Location B

Figs. 12 and 13 show Rev3D results for location B, computed with the semiempirical and composite roughness scattering models, respectively. Again, a source pulse centered at 14 kHz with length 0.125 ms, after match filtering, is used, and the wind speed is 10 m/s. A fitted JONSWAP spectrum is used for Fig. 13, with parameter values $H_s = 2.0$ m, $T_p = 8.0$ s, and $\gamma = 3.0$. At travel time about 700 ms, Fig. 12 shows sharp reverberation peaks of the same type as those noted in Fig. 9. This time as well they disappear when the composite roughness surface scattering model is used (Fig. 13).

For the measured as well as modeled time traces, reverberation seems to consist of two decaying parts: one between travel times of about 655 and 680 ms, and one after 680 ms. This is particularly clear in Fig. 13, for which the modeled results agree better with the measured ones. Both reverberation parts seem to be initiated by some propagation peaks. In modeling, the first reverberation part appears at a too high level, whereas the second part decays at a too high rate.

C. Location C

The bottom topography is rather complex in this area. While the Rev3D modeling for locations A and B is done without bottom topography variations normal to the vertical plane containing the source and the receiver, the 2-D high resolution (20 m) bottom shown in Fig. 14 is used for location C. Both the source and the receiver are deployed on seamounts at depths around 75 m.

Fig. 15 shows Rev3D results for location C. This time, the source pulse is centered at 6 kHz and its length is 0.25 ms, after match filtering. The wind speed is only 3.5 m/s. At these lower values of frequency and wind speed, compared to locations A and B, the difference between the two surface-scattering alternatives is rather small; see the dashed blue and violet curves in Fig. 5. As a result, the difference by computing surface reverberation with the semiempirical or composite-roughness scattering kernel is almost negligible, and only the latter alternative

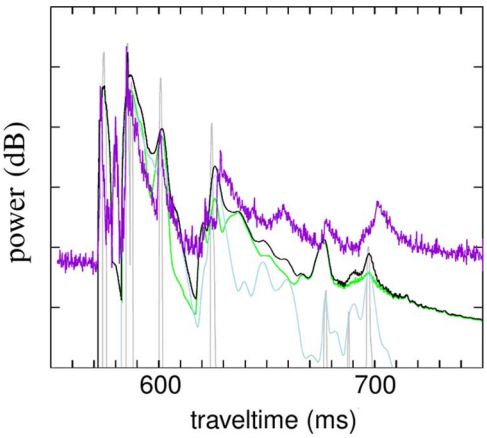

Fig. 15. Modeled and measured time series for location C, with surface reverberation modeled according to the composite-roughness scattering kernel from Section IV-D. Again, there are 10 dB between the thick marks on the vertical axis. The black, green, and blue curves represent modeled total, bottom, and surface reverberations, respectively. The gray curve represents propagation, and the violet curve shows the measured data.

is shown. No wave-rider buoy was available during the measurements at location C, and the Pierson–Moskowitz spectrum for the wind speed of 3.5 m/s is now used in connection with (5).

This time, reverberation has an interesting structure with several peaks, in the measured as well as modeled time traces. Some reverberation peaks (in violet and black) agree with modeled propagation peaks (in gray). It is interesting to compare the modeled 3-D propagation results to the corresponding 2-D results of Fig. 1. The 3-D propagation modeling captures more arrivals than the 2-D modeling, indicating the presence of out-of-plane reflections.

The modeling results are reasonably good up to travel times of about 630 or 640 ms, after which modeled reverberation drops off too quickly. Nevertheless, there is a similarity of shape at the later travel times as well, albeit with some slight time shifts for the modeled trace.

Before travel times of about 630 ms, bottom and surface reverberations are often similar in magnitude. Thereafter, surface reverberation drops off quickly at the prevailing low wind speed. After about 700 ms, modeled bottom reverberation is very smooth, and it dominates completely there.

Figs. 9, 11–13, and 15 have shown how received reverberation is distributed in time. It is also possible to study the origin in the horizontal plane of the received reverberation energy [31], [32]. Fig. 16 shows such results, per unit horizontal surface area, for modeled surface and bottom reverberations corresponding to time extensions of the blue and green curves, respectively, of Fig. 15. Particularly the surface reverberation energy density is very large near the line segment connecting the source and the receiver. Because of the source and receiver locations close to the bottom, the upward-refracting sound-speed profile, and the appearance of the bottom-scattering kernel with a weak dependence on the bistatic angle β, at least for $\beta < 135^\circ$ (Fig. 6), the contributions to bottom reverberation are more spread out.

Far away from the source and the receiver, the bottom contributions to reverberation are apparently stronger than the surface contributions in this case. This is consistent with the time traces

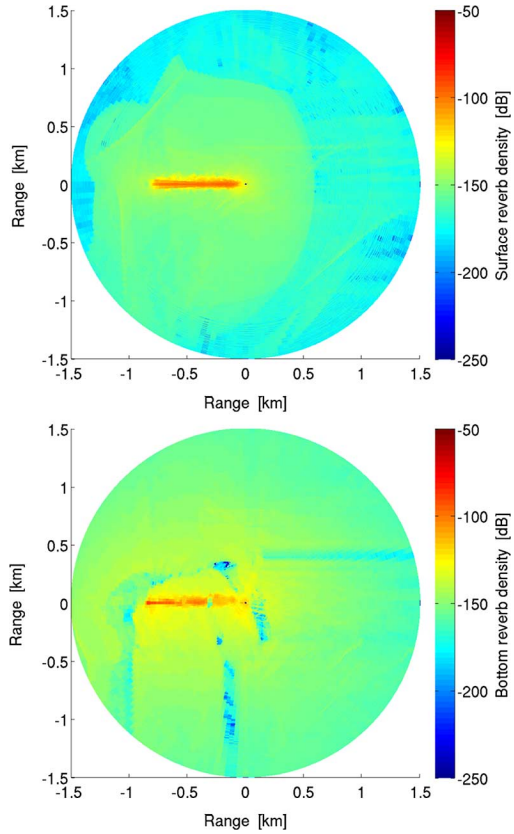

Fig. 16. Origin in the horizontal plane of received reverberation energy for location C, per unit horizontal surface area (1 m^2) and in decibels. The upper and lower panels show modeled surface and bottom reverberations, respectively. As in Fig. 15, surface reverberation is computed with the composite-roughness scattering kernel. The receiver is at the origin in the horizontal coordinate system, with the source 850 m to the left.

in Fig. 15. The bathymetry with varying depths and slopes (see Fig. 14) gives rise to some patterns in the map views. The blue regions with weak bottom reverberation appear to correspond to down-sloping bottom parts, as viewed from the line segment connecting the source and the receiver.

VI. Modeling Results With Varied Environmental Parameters

The modeling results of Section V could, of course, be improved, in terms of better fit to the measured data, by adapting the environmental input parameters within their windows of uncertainty. This section shows some additional Rev3D modeling results, where the assumed bottom porosity or the assumed wind speed is changed. Surface reverberation is now computed with the composite roughness (rather than the semiempirical) scattering kernel.

No formal inversion has been performed, and the modifications of the environmental parameters are by no means optimal. For example, at each location, the same bottom parameters are assumed all over the area, although the bottom is typically harder at outcrops than at deeper valleys where clay and mud accumulate. Nevertheless, a few examples of the sensitivity of the results to parameter changes should be of interest.

Fig. 17 shows Rev3D results for location A, where modeling is done for a harder (porosity 0.55) and more rough (ϕ equal to 8°) bottom than in Fig. 11. The propagation peaks are now

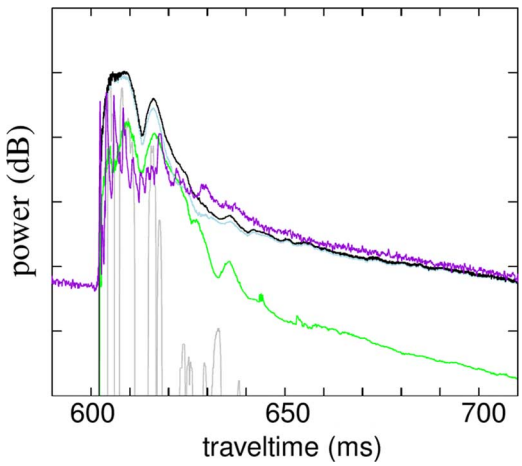

Fig. 17. Modeled and measured time series for location A, using the composite-roughness surface scattering kernel for modeling. The difference from Fig. 11 is that a harder (porosity 0.55) and more rough (ϕ equal to 8°) bottom is assumed. Again, there are 10 dB between the thick marks on the vertical axis. The black, green, and blue curves represent modeled total, bottom, and surface reverberations, respectively. The gray curve represents propagation, and the violet curve shows the measured data.

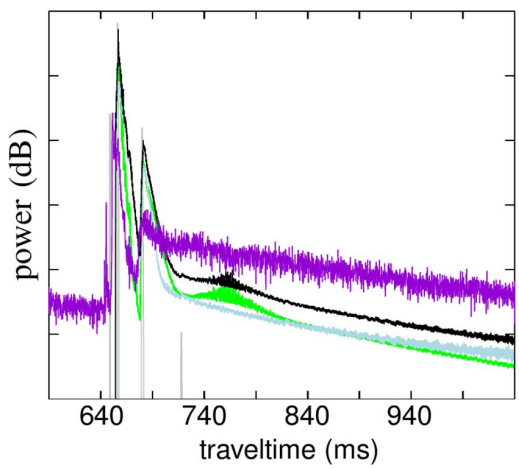

Fig. 18. Modeled and measured time series for location B, using the composite-roughness surface scattering kernel for modeling. The difference from Fig. 13 is that a smaller wind speed (7 m/s) is assumed. Again, there are 10 dB between the thick marks on the vertical axis. The black, green, and blue curves represent modeled total, bottom, and surface reverberations, respectively. The gray curve represents propagation, and the violet curve shows the measured data.

higher, except the initial ones, which do not involve the bottom. Reverberation has also increased, and for travel times longer than about 635 ms, modeled reverberation follows the measured one closely.

Interestingly, surface reverberation still dominates bottom reverberation almost completely. In comparison to Fig. 11, surface reverberation has actually increased almost as much as bottom reverberation. Surface reverberation is, of course, enhanced as well, when stronger reflections from the bottom reach the surface.

Concerning location B, it seems very difficult to achieve correct modeling of the two reverberation parts noted in connection with Fig. 13. One might anticipate that stronger reflections, induced by a harder bottom or a lower wind speed in modeling, would reduce the decay of the second part beyond 680 ms. For reasonable changes (within the pertinent uncertainty windows),

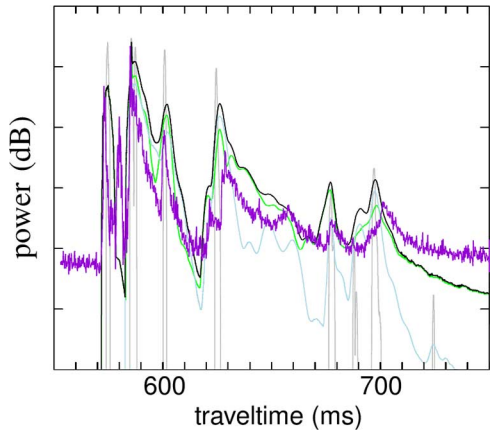

Fig. 19. Modeled and measured time series for location C, using the composite-roughness surface scattering kernel for modeling. The difference to Fig. 15 is that a harder (porosity 0.47) and more rough (ϕ equal to 9°) bottom is assumed. Again, there are 10 dB between the thick marks on the vertical axis. The black, green, and blue curves represent modeled total, bottom, and surface reverberations, respectively. The gray curve represents propagation, and the violet curve shows the measured data.

the effect seems to be too small, however. An example is provided in Fig. 18, for which the wind speed is lowered to 7 m/s in modeling. Indeed, the modeled reverberation slope is slightly reduced toward the end, but the reverberation level is still much too low there. Moreover, the levels of initial propagation peaks have increased significantly.

Fig. 19 shows the Rev3D results for location C, where modeling is done for a harder (porosity 0.47) and more rough (ϕ equal to 9°) bottom than in Fig. 15. The propagation peaks are now higher, albeit only marginally so for the initial ones. Some of the modeled propagation peaks are much higher than the measured ones, indicating that the bottom is softer locally at the corresponding reflection spots at the bottom. The modeled reverberation trace now matches the measured one better, but there is still some misalignment. As was noted in connection with Fig. 17, a harder and more rough bottom may give rise to increased surface as well as bottom reverberation.

Several of the reverberation peaks in Fig. 19, for example the late ones at about 677 and 698 ms, appear close to propagation peaks. This is not a coincidence. The corresponding eigenrays connecting the source and the receiver involve a few bottom and surface reflections, and strong forward scattering appears from bottom and surface patches near the corresponding reflection points. Indeed, Figs. 6 and 8 exhibit significantly enhanced scattering in the azimuthal forward direction (the uppermost curves for $\beta = 180°$), particularly for moderately large grazing angles.

VII. Wind-Speed Dependence of the CIR

Wind and waves affect shallow-water CIRs due to significant surface interaction. During the measurements at location A, a 1.5 day period is experienced where wind increases steadily from 3 to 12 m/s. The significant wave height H_s increases correspondingly from 0.25 to 1.1 m, and the wave spectra evolve as shown in Fig. 20. At the start of the measurement period, the wind is low, 3 m/s, the significant wave height is $H_s = 0.25$ m, and the wave spectrum shows a narrow swell component with the peak frequency of 0.12 Hz (peak period $T_p = 8$ s). As the wind starts to increase, a broad wave spectrum centered at 0.45

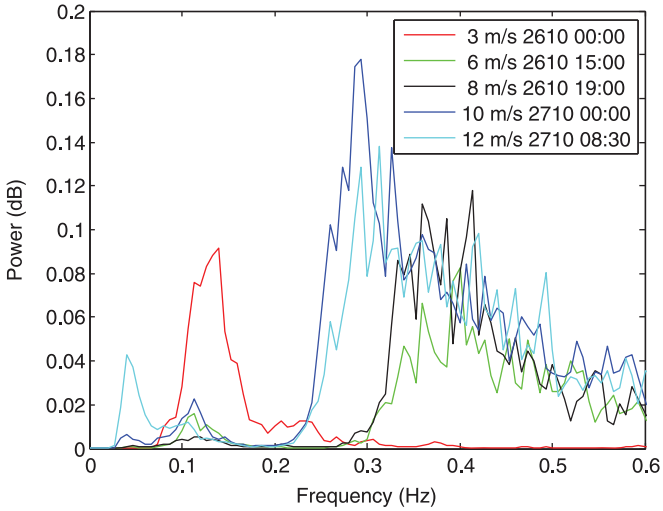

Fig. 20. Evolution of wave spectra (averaged over 20 min) versus wind at location A.

Hz appears, and with the increasing wind (and time), the spectral peak shifts toward lower frequencies while also being narrower. At 24 h after the start of the measurement, the wind speed is 10 m/s, and a well-developed wave spectrum with the peak frequency of 0.28 Hz is observed.

The evolution of the measured CIRs during the same time period is shown by the violet curves in Fig. 21. The effect of the increasing wind is mainly to shift the CIR curves down; the decay rate of the reverberant tail is virtually unchanged. Further, the propagation arrivals diminish, resulting in flatter curves.

Fig. 21 also shows modeling results, assuming the same type of bottom as in Fig. 17 (porosity 0.55, roughness slope angle ϕ equal to 8°). The shape of the modeled impulse response depends on the combined effect of reflection loss and scattering from the sea surface and the sea bottom. At low wind speeds, reflection loss and scattering from the sea surface are due to rough surface scattering. At wind speeds around 5–6 m/s, bubbles start to form, which refract, scatter, and absorb sound. At some point around 8–10 m/s [25, Sec. 8.1.1.2.2], extinction by bubbles becomes the dominant loss mechanism, resulting in increased reflection loss (cf., Fig. 4). Correspondingly, the contribution to scattering from bubbles close to the surface increases with the increasing wind speed (cf., Fig. 5).

Increasing the wind from 8 to 12 m/s, a downshift of about 8 dB is observed, somewhat more in the modeling results than in the data. The downshift is expected, since in this wind speed regime, surface reverberation dominates over bottom reverberation, and bubble extinction is the dominant loss mechanism. Bottom reverberation also decreases with the increasing wind due to higher surface-reflection loss.

While a simple downshift of the reverberation curves is expected in the high wind regime, what is surprising is the virtually unchanged slope of the tails at low wind speeds, for which a different loss mechanism dominates. Although modeling fails in estimating the correct level of the reverberation curves, it is able to shed some light on this observation. It turns out that in the low wind regime (the upper panel of Fig. 21), bottom reverberation dominates over surface reverberation; surface reverberation indeed falls off at a faster rate than for higher winds.

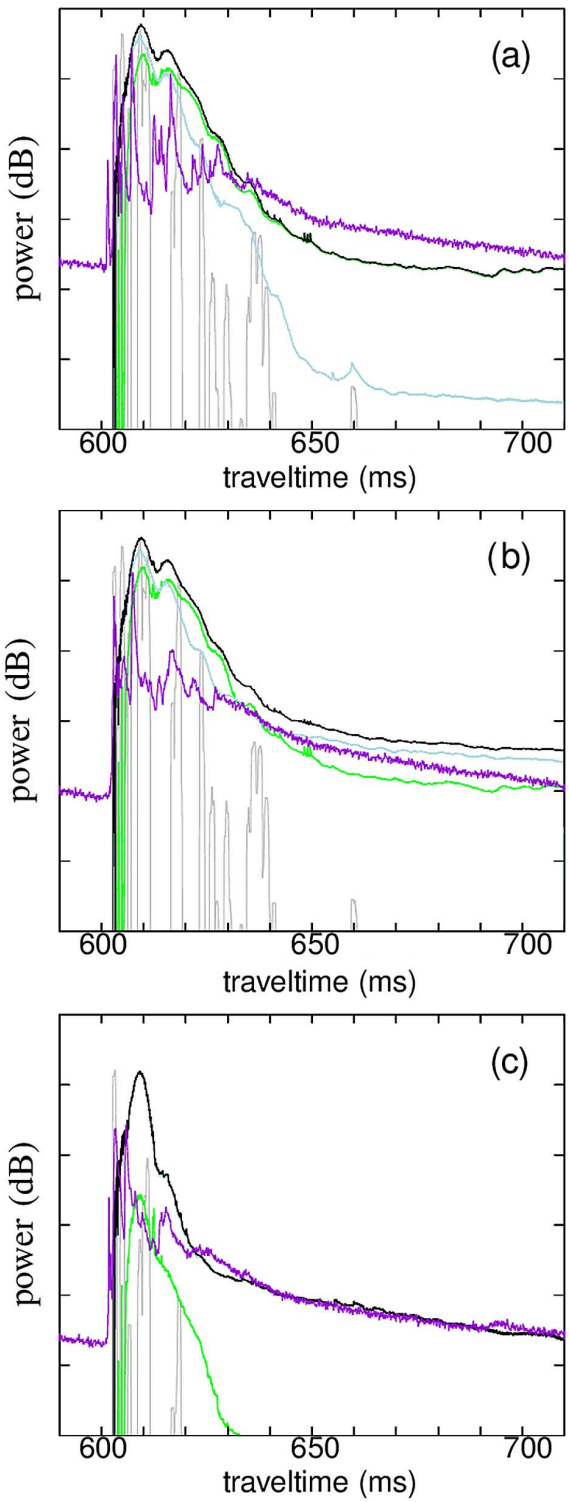

Fig. 21. Measured (violet curves) and modeled power delay profiles for location A at different wind speeds: (a) 3 m/s, (b) 8 m/s, and (c) 12 m/s. Modeling is done with the composite-roughness surface scattering kernel for the same type of bottom as in Fig. 17. There are 10 dB between the thick marks on the vertical axes. The black, green, and blue curves represent modeled total, bottom, and surface reverberations, respectively, and the gray curves represent propagation.

VIII. Conclusion

Channel simulators are useful tools for development and testing of new modulation schemes, with potential to be used much more extensively by the underwater communications society. Model-based simulators are particularly useful, as they

allow simulations of unmeasured channels, thus reducing the need for expensive sea trials. However, modeling all effects pertinent to acoustic communications in a realistic fashion is a formidable task. This paper addresses the ability to model the delay spread of the channel, and it is motivated by the following: 1) many shallow-water communication channels exhibit long continuous tails, which cannot be reproduced by 2-D propagation modeling, and 2) failure to model the complete delay profile may lead to unrealistically optimistic simulation estimates of communication performance.

The continuous nature of the impulse responses and the low correlation and slow decay rates of the tails point toward reverberation as an important mechanism behind the observations. Proper modeling thus requires the ability to compute propagation as well as reverberation in a bistatic geometry, and to include out-of-plane scattering in the computations.

A model with these capabilities is the 3-D ray model Rev3D, and it has been used in this work to investigate to what extent the long tails in the measured time series can be explained by bistatic out-of-plane scattering and reverberation. For this purpose, Rev3D has been amended in various ways. Semiempirical 3-D scattering-strength functions proposed by Ellis and Crowe [14] have been implemented for bottom as well as surface reverberation. For the surface, a version of the composite roughness surface-scattering model has also been implemented. Observed time variations in the measured data indicate that surface reverberation usually dominates, and the composite roughness model typically provides enhanced scattering at low grazing angles due to scattering by bubbles, providing a better match to the measured data.

Rev3D modeling supports the hypothesis that out-of-plane scattering and reverberation are main mechanisms behind the observed continuous, exponentially decaying impulse responses. There are discrepancies, however, due to uncertain environment, physics not included in modeling, and probably also the inability of the scattering functions to model all aspects of the present environment correctly. In particular, the scattering functions seem to overestimate early reverberation. While rough surface scattering and attenuation by wind-generated bubbles are included in modeling, Doppler effects are not, and neither are multiple scattering effects.

Ground truth knowledge of the bottom types is limited, and the first modeling efforts were made by assuming bottoms of medium porosity. By somewhat reducing the bottom porosity, reasonably good agreement of measured and modeled time series could be obtained for locations A and C. For location B, the main features of reverberation, with two decaying parts, were recovered. The measured levels and decays of the two parts were not matched by modeling, however. Variations in the sound-speed profile could be one possible explanation, and variations in bottom porosity and roughness in the area could be another. The uncertainty in modeling due to an uncertain environment applies, of course, to all three areas. As in [33], bottom porosity values for modeling could be set guided by the local bottom depth and slope.

According to modeling, sea-surface reverberation dominates at all three locations, except for some cases with very low wind speed at locations A and C. This is consistent with observations of Doppler spread in the tails. For location A, measurements as well as modeling indicates that the bottom reverberation dominated tails at very low wind speeds decay at roughly the same rate as the surface reverberation dominated tails at higher wind speeds.

The improved CIRs obtained in this work are immediately applicable in channel simulators, such as Mime [1], which take as input measured or modeled channel characterizations.

A natural next step would be to include Doppler effects in modeling. There are several approaches to model-based simulation of the effects of moving sea surfaces. The most realistic are direct simulations [7], [8], however, such simulations are prohibitive with a 3-D model. Among the simpler alternatives, which could work with 3-D models, is to assign the proper Doppler spectrum to each surface-reflected path. The approach is a static surface approximation where the effect of the surface motion is to modulate the reflection coefficients.

ACKNOWLEDGMENT

The acoustic data sets used for this study were collected by FFI and Kongsberg Maritime (KM). The authors would like to acknowledge P. van Walree and R. Otnes for many valuable discussions. K. Otto pointed out a simple way to speed up the Rev3D computations significantly. The anonymous reviewers made several good suggestions, improving the paper.

REFERENCES

[1] P. A. van Walree, T. Jenserud, and M. Smedsrud, "A discrete-time channel simulator driven by measured scattering functions," *IEEE J. Sel. Areas Commun.*, vol. 26, no. 9, pp. 1628–1637, Dec. 2008.

[2] A. Zielinski, Y. Yoon, and L. Wu, "Performance analysis of digital acoustic communication in a shallow water channel," *IEEE J. Ocean. Eng.*, vol. 20, no. 4, pp. 293–299, Oct. 1995.

[3] I. Karasalo, T. Öberg, B. Nilsson, and S. Ivansson, "A single-carrier turbo-coded system for underwater communication," *IEEE J. Ocean. Eng.*, vol. 38, no. 4, pp. 666–677, Oct. 2013.

[4] X. Geng and A. Zielinski, "An eigenpath underwater acoustic communication channel model," in *Proc. MTS/IEEE OCEANS Conf.*, Seattle, WA, USA, Oct. 1995, vol. 2, pp. 1189–1196.

[5] M. Chitre, "A high-frequency warm shallow water acoustic communications channel model and measurements," *J. Acoust. Soc. Amer.*, vol. 122, no. 5, pp. 2580–2586, Nov. 2007.

[6] X. Cristol, "NARCISSUS-2005: A global model of fading channel for application to acoustic communication in marine environments," in *Proc. IEEE OCEANS Conf.*, Seattle, WA, USA, Jun. 2005, vol. 1, pp. 655–662.

[7] M. Siderius and M. B. Porter, "Modeling broadband ocean acoustic transmissions with time-varying sea surfaces," *J. Acoust. Soc. Amer.*, vol. 124, no. 1, pp. 137–150, Jul. 2008.

[8] H. S. Dol, M. E. G. D. Colin, M. A. Ainslie, P. A. van Walree, and J. Janmaat, "Simulation of an underwater acoustic communication channel characterized by wind-generated surface waves and bubbles," *IEEE J. Ocean. Eng.*, vol. 38, no. 4, pp. 642–654, Oct. 2013.

[9] D. G. Simons, R. McHugh, M. Snellen, N. H. McCormick, and E. A. Lawson, "Analysis of shallow-water experimental acoustic data including a comparison with a broad-band normal-mode propagation model," *IEEE J. Ocean. Eng.*, vol. 26, no. 3, pp. 308–323, Jul. 2001.

[10] T. Jenserud and R. Otnes, "Reverberation tail in power delay profiles: Effects and modeling," in *Proc. OCEANS Conf.*, Bergen, Norway, Jun. 2013, DOI: 10.1109/OCEANS-Bergen.2013.6608063.

[11] P. A. van Walree, "Channel sounding for acoustic communications: Techniques and shallow-water examples," Norwegian Defence Research Establishment (FFI), Horten, Norway, Tech. Rep. 00812, 2011.

[12] R. J. Urick, *Principles of Underwater Sound*, 3rd ed. Newport Beach, CA, USA: Peninsula Publishing.

[13] S. T. McDaniel, "Sea surface reverberation: A review," *J. Acoust. Soc. Amer.*, vol. 94, no. 4, pp. 1905–1922, 1993.

[14] D. D. Ellis and D. V. Crowe, "Bistatic reverberation calculations using a three-dimensional scattering function," *J. Acoust. Soc. Amer.*, vol. 89, no. 5, pp. 2207–2214, 1991.
[15] P. H. Dahl, "On bistatic sea surface scattering: Field measurements and modeling," *J. Acoust. Soc. Amer.*, vol. 105, no. 4, pp. 2155–2169, 1999.
[16] J. W. Choi and P. H. Dahl, "Measurement and simulation of the channel intensity impulse response for a site in the east china sea," *J. Acoust. Soc. Amer.*, vol. 119, no. 5, pp. 2677–2685, 2006.
[17] P. A. van Walree, "Propagation and scattering effects in underwater acoustic communication channels," *IEEE J. Ocean. Eng.*, vol. 38, no. 4, pp. 614–631, Oct. 2013.
[18] E. Dombestein and A. L. Gjersøe, "Lybin 6.1—User Manual," Norwegian Defence Research Establishment (FFI), Horten, Norway, Tech. Rep. 2012/01463, 2012.
[19] S. Ivansson, "Stochastic ray-trace computations of transmission loss and reverberation in 3-D range-dependent environments," in *Proc. 8th Eur. Conf. Underwater Acoust.*, S. M. Jesus and O. C. Rodriguez, Eds., Carvoeiro, Portugal, Jun. 2006, pp. 131–136.
[20] F. Sturm, S. Ivansson, Y.-M. Jiang, and N. R. Chapman, "Numerical investigation of out-of-plane sound propagation in a shallow water experiment," *J. Acoust. Soc. Amer.*, vol. 124, no. 6, pp. EL341–EL346, 2008.
[21] A. L. Piskarev, "Calculation of the average intensity distributions of sound fields in the ocean," *Sov. Phys. Acoust.*, vol. 35, pp. 418–422, 1989.
[22] S. Ivansson, "Ray modelling of active sonar element-level time series in 3-D range-dependent environments," in *Proc. 1st Int. Conf. Exhibit. Underwater Acoust.*, J. S. Papadakis and L. Bjørnø, Eds., Corfu, Greece, Jun. 2013, pp. 473–480.
[23] H. Weinberg, "Navy Interim Surface Ship Model (NISSM) II," Naval Underwater Systems Center (NUSC), Newport, RI, USA, Tech. Rep. TR4527, 1973.
[24] H. G. Schneider, "Modelling wind dependent acoustic transmission loss due to bubbles in shallow water," in *Progress in Underwater Acoustics*, H. M. Merklinger, Ed. New York, NY, USA: Plenum, 1987, pp. 509–516.
[25] M. A. Ainslie, *Principles of Sonar Performance Modeling*, 1st ed. New York, NY, USA: Springer-Verlag, 2010.
[26] P. M. Ogden and F. T. Erskine, "Surface scattering measurements using broadband explosive charges in the critical sea test experiments," *J. Acoust. Soc. Amer.*, vol. 95, no. 2, pp. 746–761, 1994.
[27] M. Gensane, "Sea surface scattering strength: Theory versus experiments and Chapman-Harris formula," in *Proc. 6th Eur. Conf. Underwater Acoust.*, A. Stepnowski, Ed., Gdansk, Poland, Jun. 2002, pp. 107–112.
[28] P. Dahl, "The contribution of bubbles to high-frequency sea surface backscatter: A 24-h time series of field measurements," *J. Acoust. Soc. Amer.*, vol. 113, no. 2, pp. 769–780, 2003.
[29] "High-frequency ocean environmental acoustic models handbook," Applied Physics Lab (APL), University of Washington, Seattle, WA, USA, Tech. Rep. TR9407, 1994.
[30] K. Hasselmann *et al.*, "Measurements of wind-wave growth and swell decay during the joint north sea wave project," *Deut. Hydr. Zeitschrift*, vol. A8, no. 12, 1973.
[31] C. H. Harrison, "Fast bistatic signal-to-reverberation-ratio calculation," *J. Comput. Acoust.*, vol. 13, no. 2, pp. 317–340, 2005.
[32] C. H. Harrison, "Closed form bistatic reverberation and target echoes with variable bathymetry and sound speed," *IEEE J. Ocean. Eng.*, vol. 30, no. 4, pp. 660–675, Oct. 2005.
[33] J. Pihl, L. Abrahamsson, S. Ivansson, and J. Schön, "Mid frequency bottom-interacting sound propagation and reverberation in the Baltic," *Open Acoust. J.*, vol. 4, pp. 1–13, 2011.

Trond Jenserud received the M.Sc. degree in electrical engineering and the Ph.D. degree in telecommunications from the Norwegian Institute of Technology, Trondheim, Norway, in 1980 and 2001, respectively.

He is currently with the Norwegian Defence Research Establishment (FFI), Horten, Norway. His research interests include wave propagation, signal processing, and underwater communications.

Sven Ivansson received the Licentiate degree in applied geophysics from Luleå University of Technology, Luleå, Sweden, in 1987 and the Ph.D. degree in technical acoustics from the Royal Institute of Technology, Stockholm, Sweden, in 1994.

He has worked for more than 30 years with seismics, seismology, and underwater acoustics at the Swedish Defence Research Agency, Stockholm, Sweden, where he is currently a Research Director specializing in theoretical underwater acoustics. He has published papers on seismic tomography, theoretical and computational aspects on seismoacoustic wave fields, and phononic crystal slabs with application to anechoic coatings.

Dr. Ivansson is a member of the Acoustical Society of America.